

Oxide scale formation on 316L and FeCrAl steels exposed to oxygen controlled static LBE at temperatures up to 800 °C

C. Cionea ^{*}, M.D. Abad ¹, Y. Aussat ¹, D. Frazer ¹, A.J. Gubser ¹, P. Hosemann ¹

University of California Berkeley, Department of Nuclear Engineering, Berkeley, USA



ARTICLE INFO

Article history:

Received 8 May 2015

Received in revised form

25 August 2015

Accepted 3 September 2015

Keywords:

Solar energy

LBE corrosion

FeCrAl alloys

Oxygen control

Complex oxides

ABSTRACT

The corrosion behavior of three stainless steels (316L, Alkrothal 720 and Kanthal-APM) in static LBE with oxygen concentration of 10^{-5} wt% at temperatures of 700 °C for 230 h and 800 °C for 360 h was studied. The steel surface morphology of the oxide scales formed was investigated by SEM, XRD and Raman spectroscopy and the cross-section by SEM and EDX. A transitional inner-layer of Fe-Cr-Al oxides was found at the substrate interface and an Al-oxide outer layer on the Fe-Cr-Al alloys. Fast growing non-protective oxide scale with underlying dissolution was observed on the 316L alloy.

© 2015 Elsevier B.V. All rights reserved.

1. Introduction

Heavy liquid metals such as liquid-bismuth eutectic (LBE: 45 wt% Pb, 55 wt% Bi) with a low melting point and low vapor pressure are considered as heat transfer fluids in nuclear as well as concentrating solar power applications [1]. Both the nuclear and the solar concentrator community are concerned with an efficient and safe heat transport fluid with good thermal and fluid properties. In addition, LBE also provides excellent neutronic properties for spallation and fast reactor applications [2]. The heat capacity of heavy liquid metals might seem not competitive (0.13 J/g K for Pb) [3] but the volumetric heat capacity is rather high (1.44 J/cm³ K) and even better than for Na (1.19 J/cm³ K) which has been realized in the past in solar and nuclear applications. In fact, the argument can be made that the volumetric heat capacity is the most important factor since pipe and plant dimensions are designed by volume, not mass, and the costs scale with the size of the structure. Despite the excellent heat transport properties, the difficulty with utilizing LBE as a liquid can be found in the interaction with common structural material, namely steels. A significant amount

of research has been published involving a large number of steels [4–8] at moderate temperatures, and a few up to 750 °C [9]. While the large amount of work performed prior clearly deserves a comprehensive review this is not the purpose of this paper, instead our aim was to push the upper limit in temperature and evaluate other materials than investigated previously [10,11]. In the past it was found that active oxygen control was the key to address the corrosion phenomena as well as liquid metal contamination with oxide byproducts [12,13]. The corrosion mitigation strategy involves the growth of a protective oxide layer on the surface of the steel that will significantly reduce the dissolution of its elemental components. Since lead and bismuth oxides have a higher Gibbs free energy than that of oxides formed with the steel alloying elements, Fe, Cr, Al oxides will therefore be formed preferentially. If the oxygen concentration in the LBE can be controlled within a domain with a lower limit given by the activity of the steel oxides and the upper limit below the activity of lead and bismuth oxides, a passivation layer will always be present. This oxygen control is a function of temperature and the operational domain between the low and high oxygen will be decreasing with increasing temperature, represented by the constant oxygen concentrations lines in the Ellingham diagram [12,13].

More recent efforts have been focused on the study of corrosion behavior of Fe-Cr-Al alloys in LBE, with low Al additions (up to 6% by weight) showing improved corrosion resistance due to the formation of one of the most protective oxides which can be formed [14]. In fact Al containing coatings have been deployed via GESA surface treatment by KIT [15]. Recently the amount of Al necessary in order to form a protective oxide scale has been

* Correspondence to: Department of Nuclear Engineering, University of California – Berkeley, 1107 Etcheverry Hall, Berkeley, CA 94720, USA. Tel.: +1 510 507 4733; fax: +1 510 643 9685.

E-mail addresses: cionea@yahoo.com (C. Cionea), manueld.abad@gmail.com (M.D. Abad), yerbol@berkeley.edu (Y. Aussat), davefrazier@berkeley.edu (D. Frazer), agubser@gmail.com (A.J. Gubser), peterh@berkeley.edu (P. Hosemann).

¹ Tel.: +1 415 744 4634.

mapped out [16] and it was found that it is beneficial to have 4–5 wt% Al and 20% Cr to form a protective oxide scale [17].

The present paper shows the results of high Al containing commercial steels and their corrosion behavior in LBE at high temperatures (700 °C and 800 °C) with active oxygen control in newly build autoclaves capable to go to these temperatures and still maintain good oxygen control. We also want to emphasize the fact that we provide the actual recording of oxygen control with commercially available sensors.

2. Experimental details

2.1. Materials

One of the materials selected for this study was low carbon austenitic stainless steel 316L as a reference material to be compared with the large number of studies in which this material was tested in LBE. The other two materials included in our study were alloys from Sandvick (Kanthal): Alkrothal 720 (ALK), a ferritic Fe-Cr-Al alloy, and APM, an advanced powder metallurgical, dispersion strengthened, ferritic Fe-Cr-Al. The 316L steel was purchased in 1.5" diameter stock from McMaster-Carr, and the Kanthal alloys were provided by Sandvik in the form of 2 mm thick sheet. The steels compositions of the materials used in the corrosion tests (in wt%) are given in Table 1. Specimens were cut in rectangular coupons $20 \times 40 \times 1 \text{ mm}^3$ made to fit in a triangle layout inside an alumina cylindrical crucible 28 mm in diameter and 40 mm in height that was then filled with liquid LBE. The test samples were polished with SiC polishing paper up to 600 grit and cleaned with acetone and ethanol prior to immersing into the test crucible.

2.2. Experimental procedure

The samples were exposed to static liquid bismuth eutectic (LBE) in a custom built setup. Fig. 1 shows a schematic representation of the corrosion autoclave setup with precision environmental control. The system was built with commercially available standard stainless steel vacuum components and Swagelok tube fittings. The oxygen content was measured using commercially available oxygen sensors (purchased from Australian Oxytrol Systems) typically used for measuring oxygen in exhaust gas and smoke stacks. Their measurement principle is based on the Electromotive Force (EMF) signal between a reference (Pt-air) on the inside of the hollow YSZ sensor and the outside of the unknown liquid. Details of how the resulting EMF signal is related to oxygen concentration can be found in [18]. The standard sensors have been modified since they were delivered with a Pt wire on the outside of the sensor contacting the liquid. The Pt wire was replaced with Tungsten wires as described in [19]. The oxygen sensor was also fitted with an R-thermocouple that measures the temperature at the point of contact with the liquid metal inside the ceramic crucible. The output EMF signal from the sensor was recorded with a Keithley 181 Nanovoltmeter and together with the thermocouple signal was fed into an Omega DAQ board. A LabVIEW program was used to record experiment parameters (EMF, T,

time) as well as to control the cover gas above the corrosion setup by operating an automated valve (the on/off position being triggered by a set point in the program that would switch between pure Ar and Ar/3% H₂ mixture). It was found that a cycling of gas on/gas off around a selected set point of oxygen control maintains constant oxygen content in the liquid metal as show in in Fig. 1.

The corrosion tests were carried out at 700 and 800 °C for 230 and 360 h in static LBE. The oxygen concentration was maintained at an average 10^{-5} wt% within 0.3 order of magnitude precision (Fig. 2a). This particular oxygen concentration was chosen based on the oxygen activity of iron oxide represented by Gibbs free energy according to Ellingham diagram that will provide just enough oxygen for iron oxide to format the testing temperature. While the approach discussed above worked very well at 700, it was found that at 800 °C the tungsten wire conducting the signal failed frequently and needed to be replaced causing some thermal cycling due to the replacement of the failing tungsten wire attached to the oxygen sensor. It was found that the set oxygen content in the system causes the tungsten wire to oxidize at these temperatures, leading to failures. The procedure for the replacement of the wire was as follows: the system temperature was dropped to 300 °C and the sensor was removed for a few minutes, the time needed to replace the broken W wire. The reason the temperature was lowered was to reduce the oxygen solubility in the LBE during this process so the experiment can continue faster after the process. As a result of the above mentioned tungsten wire failure due to oxidation, the system was restarted 2 times during the 360 h total samples exposure. During the sensor removal procedure, oxygen inside the setup increased temporary to its LBE saturation limit and each time at restart a transition period of 1–2 h was required for the Ar+H₂ gas mixture to reduce the oxygen down to preset conditions. Fig. 2 shows the oxygen concentration and temperature evolution during the 700 and 800 °C tests.

After testing, the samples were removed from the LBE and prepared for post corrosion analysis. A segment of about 5 mm length was cut from each tested sample and mounted in epoxy

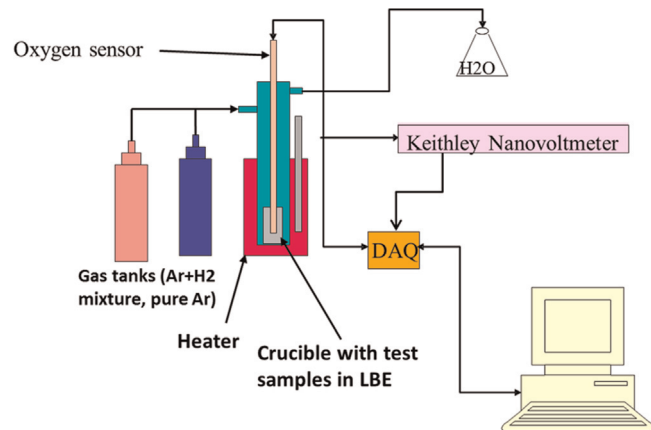


Fig. 1. Experimental setup for corrosion of steel samples in LBE.

Table 1

Standard chemical composition of the investigated steel grades (in wt%).

Alloy description	Cr	Ni	Al	Mn	Mo	Si	Ti	S	C	Fe
316L	16–18	10–14	–	<2	2–3	<1	–	<0.03	<0.03	bal.
ALK	12–14	–	4.0	0.7	–	0.7	0.25	–	0.08	bal.
APM	20–23	–	5.8	0.4	–	0.7	–	–	0.08	bal.

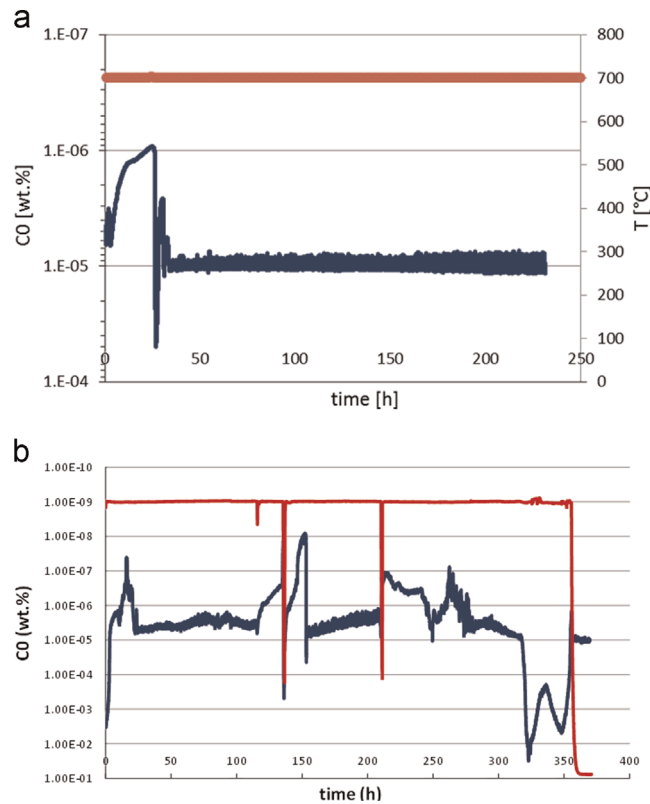


Fig. 2. Characteristic oxygen concentration and temperature versus time plot for the (a) 700 °C/250 h and (b) 800 °C/400 h corrosion test.

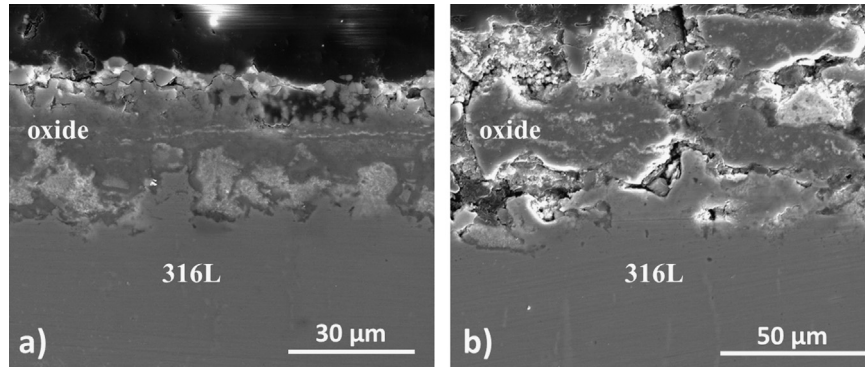


Fig. 3. SEM cross-section of the oxide scale grown on 316L at 700 °C/250 h (a) and 800 °C/400 h (b); the oxide will spall off during thermal cycle.

resin for cross sectional analysis. The mounted samples were polished with SiC paper up to 1200 grit, then 1 μm and 0.3 μm alumina suspension was used for final polishing steps. Samples were cleaned in an ultrasonic bath with acetone and ethanol then sent for analysis. The cross-section analysis was performed using a scanning electron microscope (SEM). A second segment was cut from the tested samples and the pre-existing LBE from the surface was removed using a solution of hydrogen peroxide, acetic acid and ethanol in a 1:1:1 ratio. The cleaned samples were washed in ethanol, dried and sent for surface imaging in SEM and analysis by x-ray diffraction (XRD) and Raman spectroscopy.

2.3. SEM/EDX/XRD and Raman measurements

A Quanta 3D field emission gun (FEG) scanning electron microscope with focused ion beam (SEM/FIB) has been used in this research. Energy dispersive spectroscopy (EDS) was carried out using an Oxford EDS attached to the SEM/FIB. XRD of the sample

was complete with a Bruker D8 Advance Powder x-ray diffractometer in Bragg–Brentano geometry (θ - θ setup) using Cu K α radiation (1.54 Å). A Renishaw Invia Laser Raman spectrometer was used for the characterization. The excitation wavelength used was 488 nm line of an Ar⁺ ion laser at an incident power of 10 mW. The area was analyzed using a 2 μm diameter spot through a standard \times 20 microscope objective. The spectra were collected with a 10 s data point acquisition time, a spectral range of 200–1000 cm⁻¹ and a spectral resolution of 2 cm⁻¹.

3. Results

3.1. 316L

Fig. 3a shows the SEM cross-section of the 316L sample exposed to LBE for two different conditions: at 700 °C for 230 h

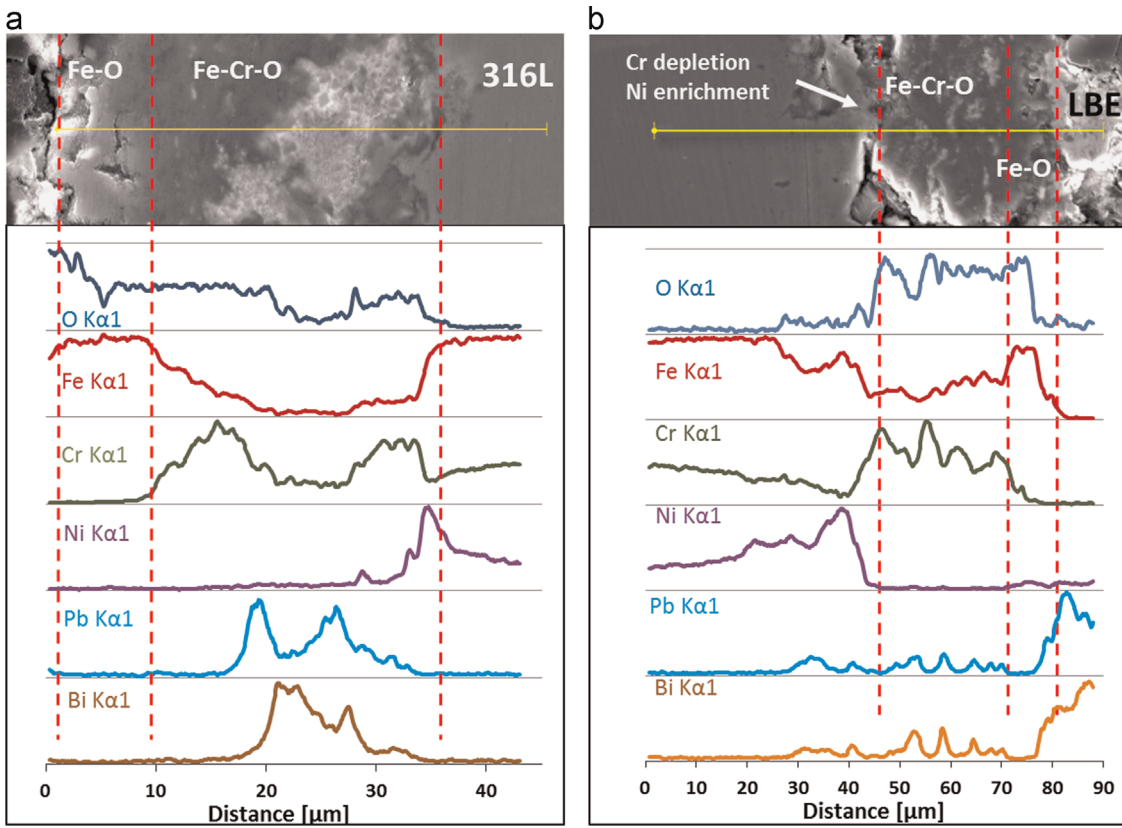


Fig. 4. EDX line scan on the oxide scale formed at 700 °C (a) and 800 °C (b) on 316L.

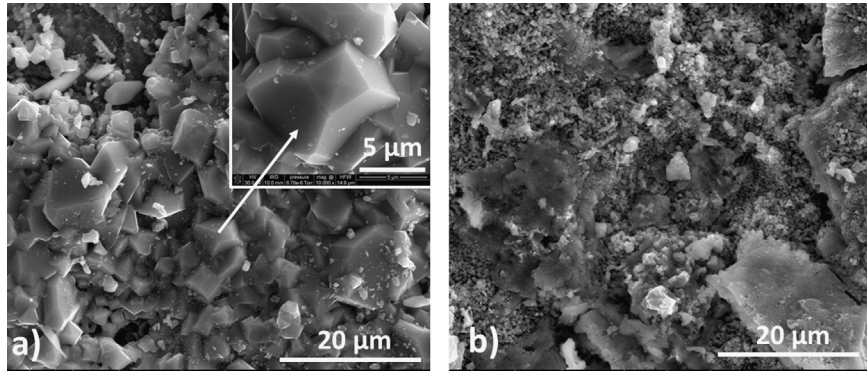


Fig. 5. Surface SEM image of 316L after exposure to LBE at 700 °C (a) and 800 °C (b).

and at 800 °C for 360 h (with two thermal cycles). After 230 h at 700 °C, a continuous 35 µm thick oxide scale was observed. EDS line scans (Fig. 4a) show that the oxide consists of a duplex layer, composed of a 10 µm thick outer layer of iron oxide on top of a Fe–Cr–O structure with rich Cr composition. A Ni rich inner layer was found at the interface between substrate and the oxide. Surface SEM images of the surface cleaned from LBE are shown in Fig. 5a. The morphology is similar to what was found in [17] and identified as magnetite. EDS elemental composition acquired of the top layer (not shown) at selected areas found 40 at% Fe and 60 at% O, consistent with the magnetite Fe/O ratio. EDS mapping of the cross-section area corresponding to the inner layer shows a ratio Fe–Cr–O characteristic to the spinel structure with a rich Cr composition.

Analysis of the 316L sample tested at 800 °C shows extensive cracking and localized delamination of the oxide layer (Fig. 3b) with extended areas where the oxide scale breaks off and a

reformed 30 µm thick oxide scale is present. The elemental EDS composition (Fig. 4b) shows a well-defined, 5 µm thick porous iron oxide layer with trace amount of Ni. Surface SEM images of the LBE-cleaned samples show plate-like structures with extended areas where the oxide scale breaks off and a renewed oxide scale about 25 µm thick was observed. Elemental composition (at%) of the surface layer probed by EDS found a ratio Fe:Cr:O of 1:1:2. The fact that Cr was found suggests that the top layer of iron oxide is thinner than the EDS excitation volume and therefore the composition was averaged over both oxide layers. Both samples show Ni enrichment as well as Cr depletion at the steel-inner oxide interface. The top surface SEM image of the rough morphology after cleaning is shown in Fig. 5b.

The samples tested at 700 °C and 800 °C were analyzed by XRD together. The original steel and the diffractograms are plotted in Fig. 6a. The original steel just shows the typical peaks from the austenitic phase of the Fe (JCPDS 52-0517). The XRD of the sample

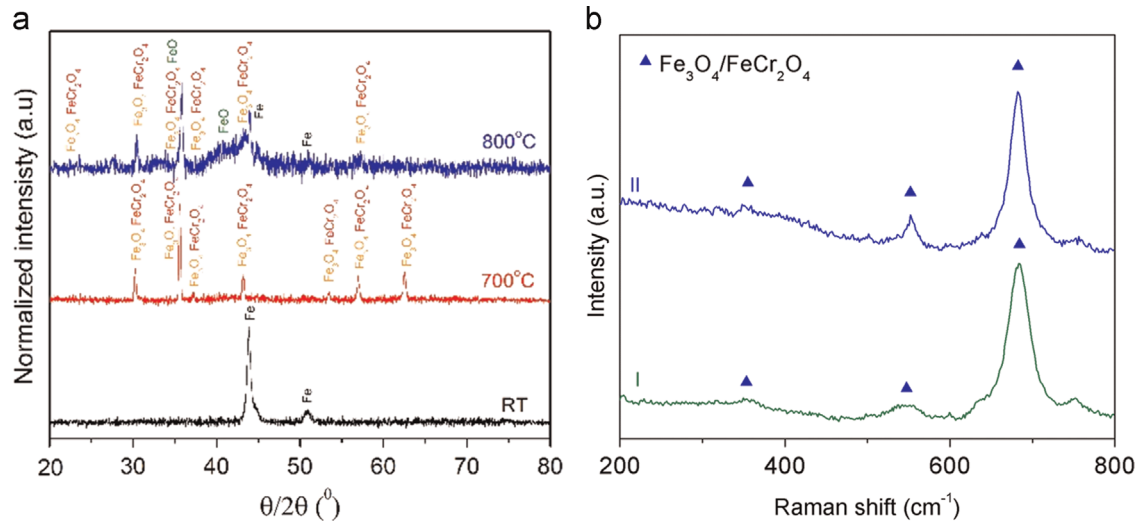


Fig. 6. a) XRD of 316L steel at RT and after the test at 700 °C and 800 °C. b) Raman spectra of the sample after 800 °C.

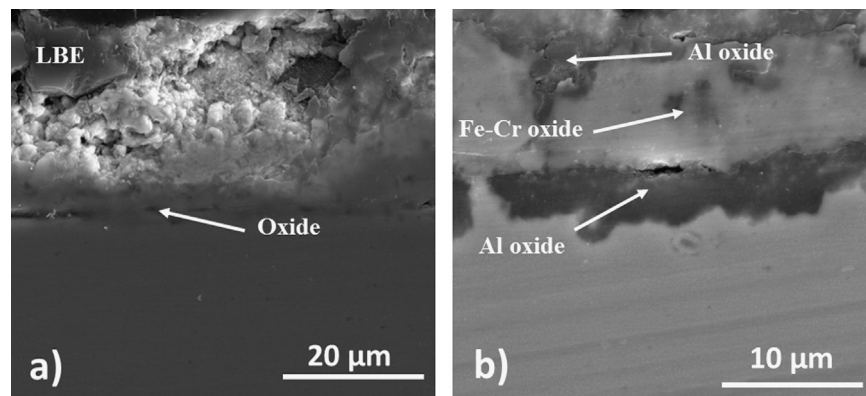


Fig. 7. SEM cross-section image of the oxide grown on ALK steel during corrosion testing in LBE at 700 °C (a) and 800 °C (b).

tested at 700 °C clearly shows the presence of the spinel-type structure, corresponding to the oxide scale and identified as magnetite Fe₃O₄ (JCPDS 74-1909) and/or chromite FeCr₂O₄ phases (JCPDS 34-0140) respectively. Utilizing the lab scale XRD one cannot distinguish between the two spinel structures due to the small differences of the pattern. It is noticed here that the oxide layer is so thick that the austenitic phase could not be detected. The XRD analysis of the sample tested at 800 °C showed the diffraction of the Fe₃O₄/FeCr₂O₄ peaks together as a broad band that could be attributed to both amorphous Fe-O oxides and the wustite FeO phase (JCPDS 79-1969). The Fe substrate could be detected due to the partial delamination of the oxide layer. The Raman spectra in Fig. 6b show the typical bands associated with the A_{1g} and T_{2g} vibration modes at 681 and 553 cm⁻¹, respectively, and a small peak at 354 cm⁻¹, from the Fe₃O₄ magnetite [21], however the biggest Raman band is slightly shifted to higher frequencies than the theoretical values for the same A_{1g} vibrations mode, 670–672 cm⁻¹ [21–24]. The reason for the shift could be a mixture of Fe₃O₄ and FeCr₂O₄ or any other non-stoichiometric Fe_{2-x}Cr_xO₃ compounds [22,25,26].

3.2. ALK

ALK alloy samples developed a rather thin and protective alumina layer for both testing conditions which is in agreement with other recent studies [26]. Fig. 7 shows representative cross-section images and Fig. 8 shows the SEM/EDX line scan of the ALK sample

after 700 and 800 °C testing. With the 700 °C sample in Fig. 8a, EDS line scan profiles show an outer layer of thin (~1 µm) Al oxide that exhibits strong and well defined peaks of Al and O. An inner-layer around 3 µm thick defined by Cr, Fe, Ti and O peaks was also identified. Fig. 9 shows representative SEM images of the sample surfaces after they were cleaned of LBE from testing conditions. The characteristic surface morphology of the sample after 700 °C (Fig. 9a) is that of a uniform scale (lighter contrast in the SEM image) comprised of small (1–2 µm) nodular grains. There is evidence of localized spallation (“islands” of oxide scale less than 300 µm wide) represented by the dark contrast in the SEM image. EDS mapping shows identical chemical compositions for both dark and light contrast regions. EDS line scans across the nodular grains show high Al, Ti, and O intensity which indicates the presence of a mixture of Al and Ti oxides structure. The ALK composition contains a small amount of Ti (Al to Ti ratio is 8:1) which explains the Ti oxide presence.

Surface SEM image of the 800 °C sample after cleaning the residual LBE (Fig. 9b) shows continuous scale morphology with nodular grains similar with that of the 700 °C sample surface. At higher magnification, two different features can be distinguished: a 5 µm size nodular and a secondary needle-like structure. An EDS spectra (Spectrum 1) from the nodular area is shown in Fig. 9b. Al, Ti and Fe are the main elements identified. Spectrum 2 shows an EDS of the needle-like structure. Al and Fe are also the main identified peaks, with less amount of Ti in this region.

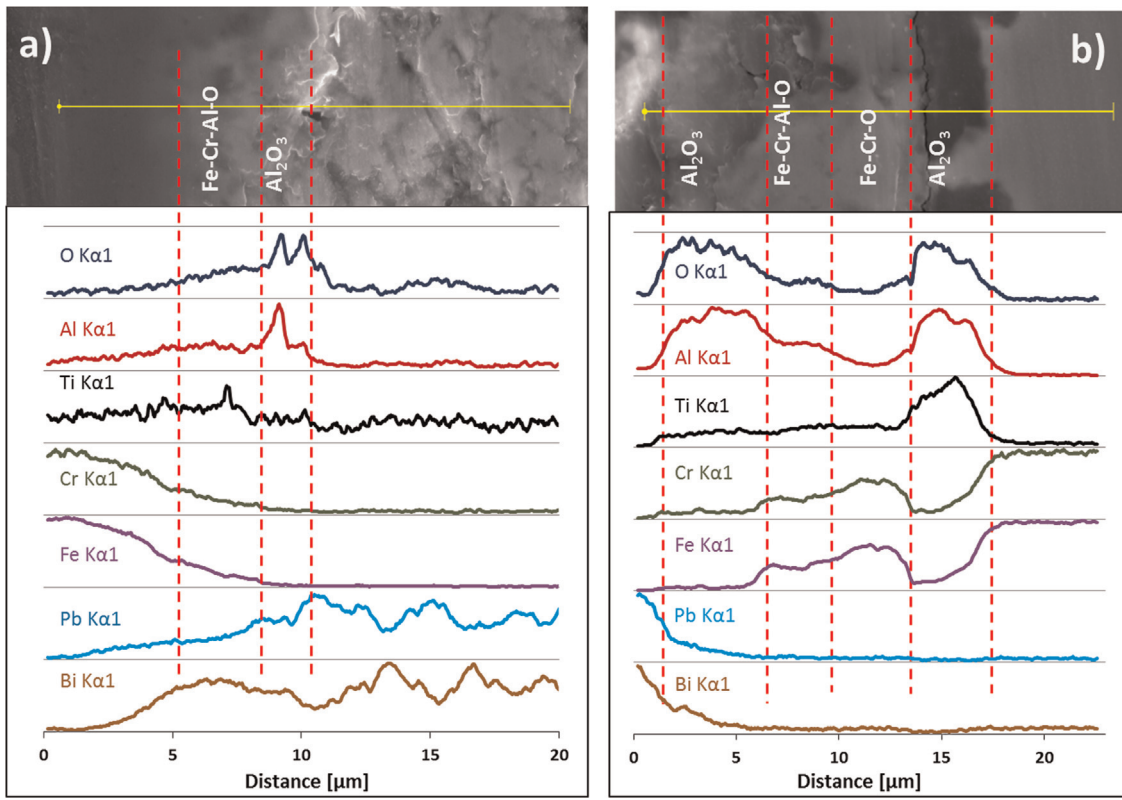


Fig. 8. SEM/EDX line scan of the ALK sample exposed to LBE at 700 °C/250 h (a) and 800 °C/400 h (b).

The diffractograms of the samples after testing at 700 and 800 °C together with the original sample (before test) are plotted in Fig. 10. At room temperature, just the ferrite Fe (JCPDS 06-0696) could be detected. At 700 °C, the diffraction from the ferrite Fe (JCPDS 06-0696) and some peaks that attributed to the diffraction of the α -Al₂O₃ (JCPDS 46-1212) are observed. The peaks of the oxides are slightly shifted to higher angles, but it is attributed to the significant stress of the oxide coating and probably due to the rapid solidification [27].

The sample tested at 800 °C shows a more complex oxide structure (Fig. 7b); there are two well defined Al oxide layers, a dense layer at the inner interface with the substrate with a darker contrast and an outer layer at the outer interface with the LBE, and a FeCrAl oxide in between them. Attending to the EDS line scan of Fig. 8b, a layer with a thickness of about 21 μm is observed. Several oxide layers were observed as follows: closer to the steel, an Al oxide layer with a large amount of titanium (~5 μm), followed by a 6–7 μm thick Fe-Cr-Al oxide, and finally, a layer of Al oxide (~5 μm) close to the LBE. Localized discontinuities in the inner Al oxide layer were found. Traces of Pb and Bi were found within the outer Al-oxide. This Al-oxide layer showed higher amount of Ti than the Al-oxide inner layer. It could explain the different in contrast observed clearly in Fig. 7b. The number of counts in the EDX line scan in Fig. 8b for the Fe-Cr-Al-O layer show an identical upward trend of Al and O and downward trend for Fe and Cr while both Al:O and Fe:Cr ratios are constant. Based on this observation, it is likely that the diffusion layer is composed of a mixture of Al₂O₃, TiO₂ and Fe-Cr oxide spinel with a composition gradient.

The XRD measurements of the sample tested at 800 °C (Fig. 10a) showed a mixture of different oxides. The diffractogram is quite complex due to the large number of peaks observed and the potential strain in the oxide layers. In an attempt to identify the peaks, aluminum (JCPDS 46-1212 and 04-0878), chromium (JCPDS 5-4552) and titanium (JCPDS 21-1276 and 21-127) oxides are labelled. In addition to SEM and XRD we also conducted a

Raman study of the surface after exposing the samples to LBE at 800 °C. The Raman spectra (I–IV) in Fig. 10b from the sample surface indicate a complex structure. Spectra I shows bands at 306, 350 and 550 cm⁻¹ that could be attributed to the Cr₂O₃ phase [28]. The peak with the highest intensity at 675 cm⁻¹ is attributed to Fe₃O₄/FeCr₂O₄ [21,28]. Spectrum II shows bands at 219, 276, and 676 cm⁻¹ and a small shoulder at 718 cm⁻¹. Similar spectra can be attributed to FeCr₂O₄ [24]. Spectrum III showed a band at 677 cm⁻¹ and a pronounced shoulder at 713 cm⁻¹. The high intensity of the shoulder suggests the formation of FeCr₂O₄ [24]. However it is also believed that the biggest peak could be attributed to the Fe₃O₄ phase. Moreover, small peaks at the Cr₂O₃ position were observed. Spectrum IV shows the typical bands observed in rutile phase (TiO₂). The bands at 610, 440 and 240 cm⁻¹ are associated to the A_{1g}, E_g, and second order effect respectively from the Rutile phase [29–31]. Similar spectra were found by Fei et al. in a study of the oxidation of Ti in Kanthal AF [32]. Al₂O₃ was not found by Raman spectroscopy in this study which could be based on either that (i) the signal of alumina was much weaker compared to that of TiO₂ or the iron and chromium oxides [32], or (ii) amorphous Al₂O₃ or another metastable alumina phase with a rather low degree of crystallinity has been grown.

3.3. APM

A thin oxide was observed using SEM cross-sectional specimens of the Kanthal-APM alloy exposed to 700 °C in LBE (Fig. 11a). EDX line scans across the oxide layer show a two-layered structure. Each layer is found to be ~2 μm thick, with an outer layer of Al-oxide and an inner layer of Fe-Cr-Al oxides. Isolated Al and O peaks within the LBE show that a free-floating Al-oxide scale was present within the LBE. Fig. 13a shows the LBE-cleaned surface, in which the dark contrast regions were attributed to Al oxide (noticeable increase in Al and O

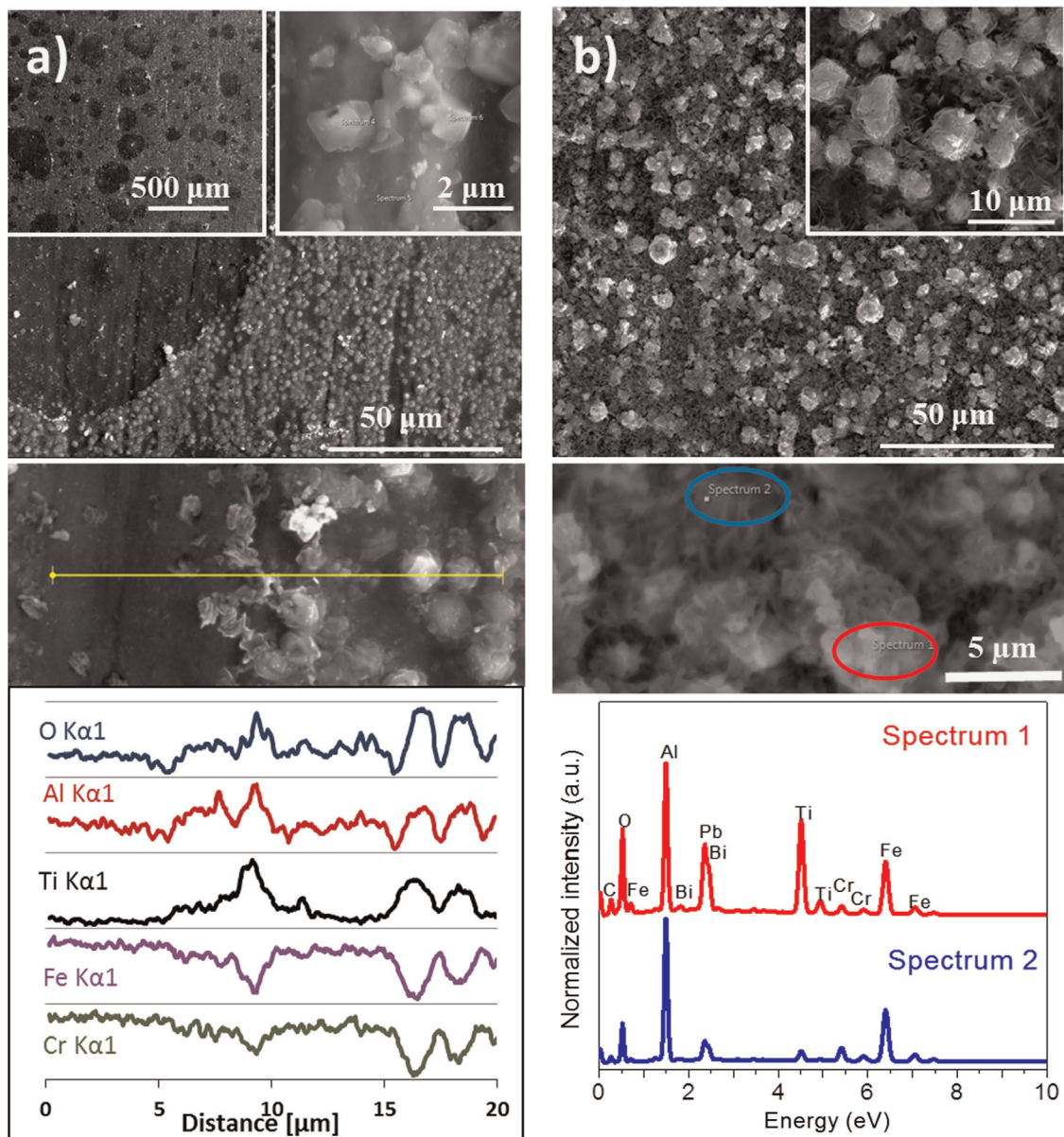


Fig. 9. Surface SEM image of sample ALK after exposure to LBE at 700 °C (a) and EDX line scan of a higher magnification area; and SEM image after test at 800 °C (b) together a higher magnification image with EDS spectra of selected areas.

composition line scans). The surface that was not covered by the oxide developed pit-type dissolution.

After 800 °C exposure, an oxide layer structure composed of a 6 μm outer layer of aluminum oxide and a submicron size inner layer of Fe–Cr–Al oxides was found (Figs. 11b and 12b). The outer Al-oxide scale shows extensive to full delamination along the interface to the inner formed oxide as well as transversal fractures within the layers with LBE penetration between loose oxide segments. Fig. 13b shows the sample surface after the LBE was etched away. The exposed steel surface shows significant dissolution with two alternating morphologies, a corral-like structure and a plate-like structure that will be discussed further below. The corresponding EDS line scans of the patches covering the sample show Al and O rich, similar to 700 °C observations. Fig. 14 shows the XRD data taken from the APM sample before and after LBE corrosion tests. The three diffractograms look rather similar where the biggest diffraction peak comes from Fe-ferrite (JCPDS 06-0696) and some small peaks attributed to the α -Al₂O₃ (JCPDS 46-1212).

4. Discussion

While the oxide layers found on the three steel samples are in agreement with previous reported results, there were several notable differences that were the result of the specific testing conditions characterized by exposure to thermal cycling. Fig. 15a presents the average oxide thickness layers observed after the testing at 700 and 800 °C. To our knowledge, there is no available data that takes into account a thermal cycling of LBE exposed Fe–Cr–Ni and Fe–Cr–Al alloys. However, we do think that this is rather important in respect to solar power. A complex oxide layer was found on the samples exposed to high temperature LBE with 3 thermal cycles.

The 316L material was chosen as a control sample for the tests conducted. There is a wide range of available data for the LBE corrosion at temperatures up to 750 °C [20,33,34]; however this is the first time that 800 °C tests have been reported. Based on our acquired experience, the solution that will prevent the repeated restarting will be to employ a different conductive material, not

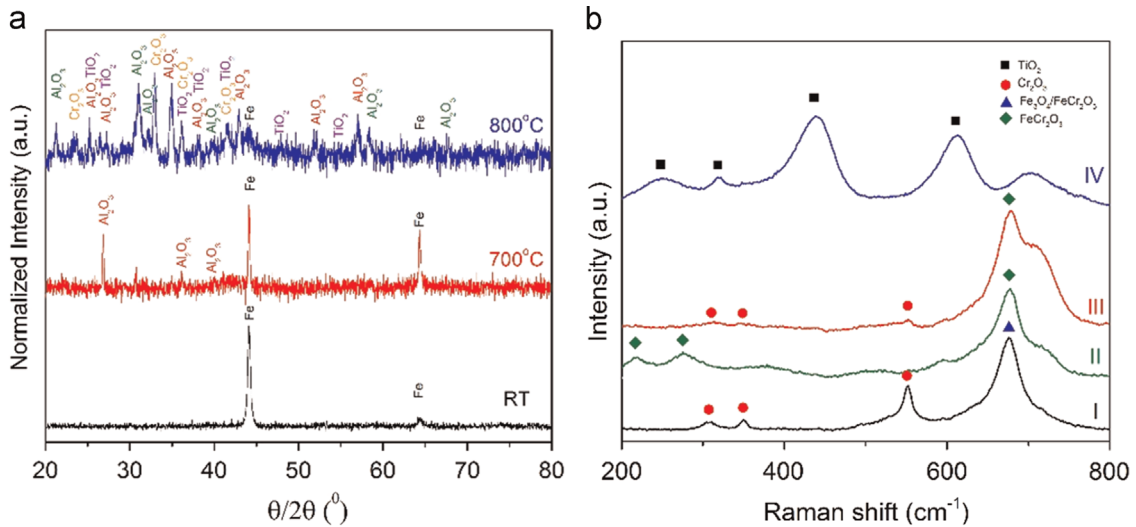


Fig. 10. (a) XRD of sample ALK at RT and after exposure to LBE at 700 °C and 800 °C. (b) Raman spectra from sample after test at 800 °C.

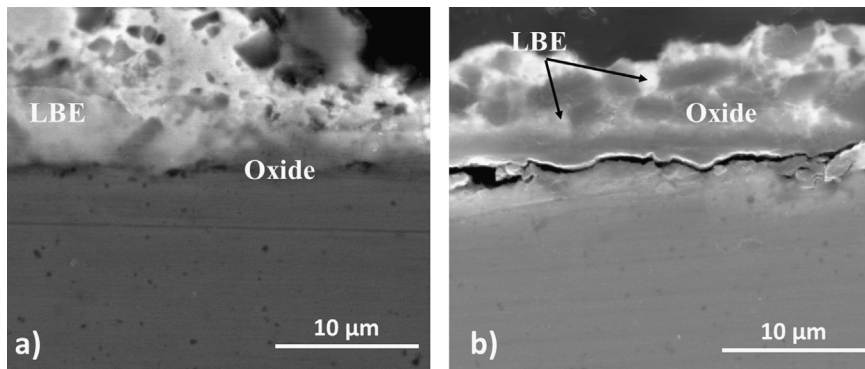


Fig. 11. SEM cross-section image of the oxide scale grown on APM steel during corrosion testing in LBE at 700 °C (a) and 800 °C (b).

soluble in LBE, which will be used as a bridge between the oxygen sensor's Pt wire and the LBE at the point of contact between the electrode and the LBE.

The most evident difference in 316L oxidation behavior is the change in surface morphology. In the 700 °C test, the surface shows evidence of a granular structure. Based on the morphology, the EDX and the XRD data, we identified this oxide as magnetite. However, the formation of FeCr_2O_4 could not be discarded. In fact, it is believed that both oxides were formed, with the Cr mostly in the inner part of the oxide layer. After 800 °C, the characteristic surface feature was a thin and plate-like morphology that has been often attributed to magnetite; however the study of the surface by XRD showed the formation of Fe_3O_4 and an amorphous Fe–O layer that could be attributed to the formation of FeO . The formation of the less stable FeO versus magnetite could be the result of the repeated thermal cycling as well as the increased oxygen exposure during the restarting procedure.

The oxide layer thickness at 700 °C/230 h was ~35 µm, while the 800 °C/360 h oxide layer average thickness was 30 µm. Both oxide scales were found to not be protective with LBE penetration. The total delamination of the grown oxide was due to the thermally induced stresses as well as poor bonding caused by LBE infiltration. As a result of this oxide evolution mechanism, the scale found on the 800 °C sample could be considered as being formed during the final thermal cycle. The oxide breakoff was expected after the thermal cycling; however it was worth to point out the similarities between the two oxide layers thickness. EDS composition profile in Fig. 4 showing trace amounts of Ni in the

Fe–O outer layer was the result of Ni containing LBE infiltration into the porous magnetite top layer. Since the top oxide was formed during the last thermal cycle event, it can be expected that significant amount of Ni was already present into LBE. This is in agreement with the Ni peaks within the LBE trapped inside the spinel inner layer for the 700 °C test. LBE that was found trapped within the Fe–Cr spinel layers shows no evidence of communicating channels to the surface which suggest fast LBE penetration at the onset of oxidation.

The protective scale mechanism for ternary alloys such as Fe-Cr-Al has been known for a long time (Wagner [36]). At low Cr concentrations or in the absence of Cr, the Fe-Al compound with access to oxygen would form rapidly growing outer layer oxides of Fe and internal precipitation of Al-oxide. When Cr is present at around 20% in Fe, protective Cr-oxides would form at a steady rate. When Al is added to the Fe-Cr, the Cr-oxide scale would rapidly reduce oxygen activity and diffusion at the alloy/oxide interface and would allow the lower concentration Al to reach the alloy interface with the Cr-oxide and form a dense, slow growing and protective Al_2O_3 . Although this mechanism was initially observed for gas environments, the static LBE can reproduce the same oxide evolution given the optimal conditions, such as an oxygen concentration above the corresponding Gibbs free energy of formation for the oxides of steel components that can be found in Ellingham diagrams for a given temperature that will be maintained constant during the corrosion tests. The addition of Ti has also been reported as a precursor of Al_2O_3 by Young [37]. Fe-Cr-Al alloys have the tendency to form complex oxide scales [38] after being

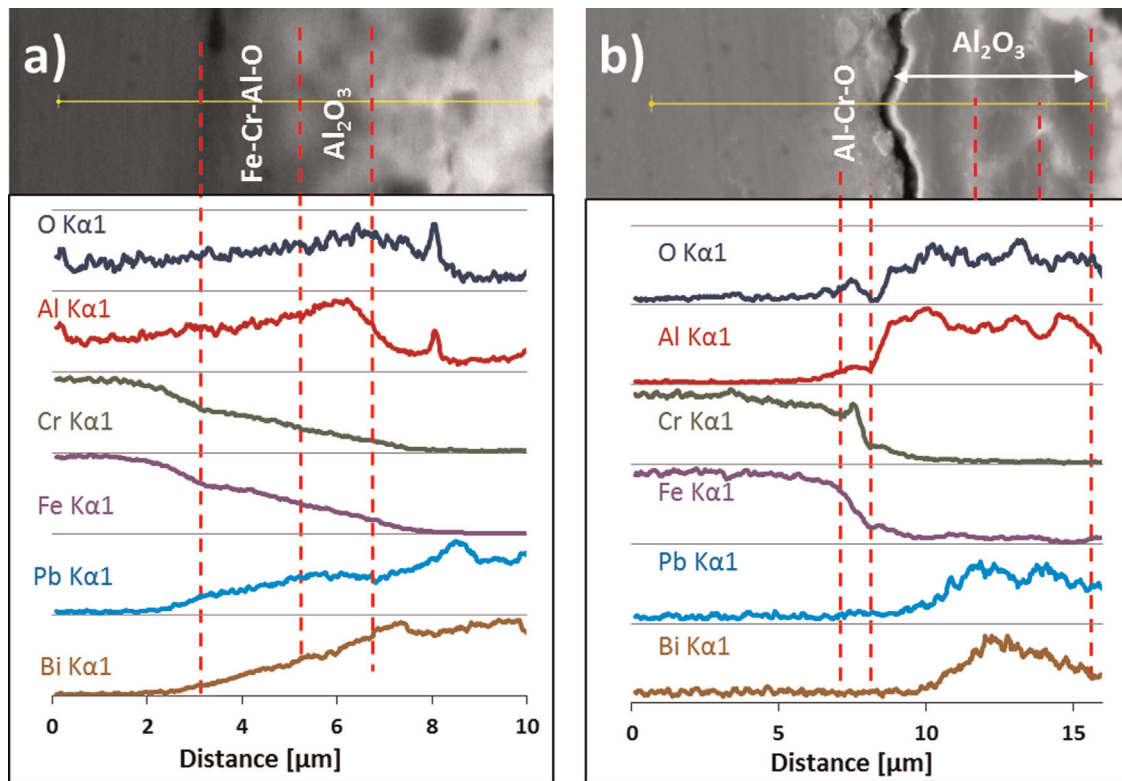


Fig. 12. EDX elemental composition of APM steel exposed to LBE at 700 °C (a) and 800 °C (b).

exposed to LBE corrosion and the stability of the Al-oxide plays a key role in the protection mechanism. Of significant importance are the oxygen concentration and the temperature. This work objective was to bridge a gap present in reported testing conditions in order to evaluate two Fe-Cr-Al alloys. The expectation was that for the relative high oxygen concentration of 10^{-5} wt% and a higher temperature (800 °C) compared to previously reported studies that focused on temperatures up to 750 °C [1,35], enhanced kinetics may produce different oxides and induce significant thermal stresses that could affect the integrity of the these oxides. Fig. 15 shows a break-down by testing conditions of the oxide layers thickness for the 316L and the Fe-Cr-Al alloys investigated. The difference in thickness of the different grown oxides is noticeable. Interestingly, at 700 °C the sample with the slightly lower Al content (sample ALK) shows the thinner Al₂O₃ layer (1 μm) in comparison with the sample APM (2 μm), which has the higher Al content. An inner layer Fe-Cr-Al-spinel type oxide with variable thickness was found at 700 °C as well as 800 °C. This Fe-Cr-Al oxide scale located at the inner-surface between the steel substrate and the outer oxide was previously reported at lower temperatures (500 and 600 °C) for an identical steel composition [26]. In recent published results [16] on similar composition alloys, the complex oxide growth rates for lower temperatures (400–600 °C) show a significant dependence on temperature and less of a dependence on exposure time. Our tests show a similar correlation for ALK and APM. The spinel-type inner oxide grows faster on the lower Cr and Al steel (ALK) at 700 °C. The higher Cr and Al steel (APM) will form oxides that will reduce the inward oxygen diffusion from LBE required for the inner layer to continue growing. The EDS line scan compositions for Ti suggest that it agglomerates around the Al oxide. The Ti peak distribution across the cross-section in Fig. 8b gives some clue about its distribution, along with Al-oxide outer boundary. The presence of Fe and Cr was the result of the X-ray interaction volume that is wider

than the Al₂O₃ layer (~1 μm) and extends through the Fe-Cr-Al oxide inner layer.

The Al₂O₃/TiO₂ inner oxide layer grown at 800 °C on the ALK sample is noticeable. A strongly beneficial effect of titanium in promoting α -Al₂O₃ formation was reported by Young [37]. Prasana et al. [42] showed that titanium from the 0.1 at% of Ti alloy was incorporated into the oxide. Pint et al. [43] suggested that Ti⁴⁺ could have the same effect as Mg²⁺, as shown by Burtin et al. [44], in accelerating the formation of α -Al₂O₃.

During the frequent unscheduled shut downs caused by failed oxygen sensors the temperature was lowered to 300 °C. The delamination and transversal fracturing of the Al-oxide was likely caused by the phase changes and thermally induced stresses. It has been shown that stable α -Al₂O₃ is the result of metastable transient phases present at lower temperatures (400 °C–600 °C) [39] that have a higher growth rate and induce a volume change of around 14% by the transformation from γ to α -Al₂O₃ [40]. The very thin (1 μm) inner oxide formed on APM at 800 °C was the result of final thermal cycling during which the previously former passivation layer fractured and the unprotected underlying complex oxide was lost. The surface morphology images gave a good assessment of the extent of dissolution at the delamination zones. ALK showed superior protection compared to APM. Previously reported [41] surface analysis of the oxide layer of FeCrAl in LBE with saturated oxygen found an identical surface morphology and Al₂O₃ layer with the ALK sample. Not only ALK surfaces had significantly less area Al-oxide delamination (about 50 at% versus 90 at% in case of APM), but the lack of dissolution pits on ALK sample would indicate that the Fe-Cr-Al-oxide inner-layer provided additional protection when the Al₂O₃ was not present and acted as a passivation layer (for all tests except the 800 °C APM). Fig. 12b shows the formation and growth of the Fe-Cr-Al-oxide; Cr and O peak overlapping indicates a Cr-rich oxide layer that forms at the early stage of exposure, followed by Al outward diffusion.

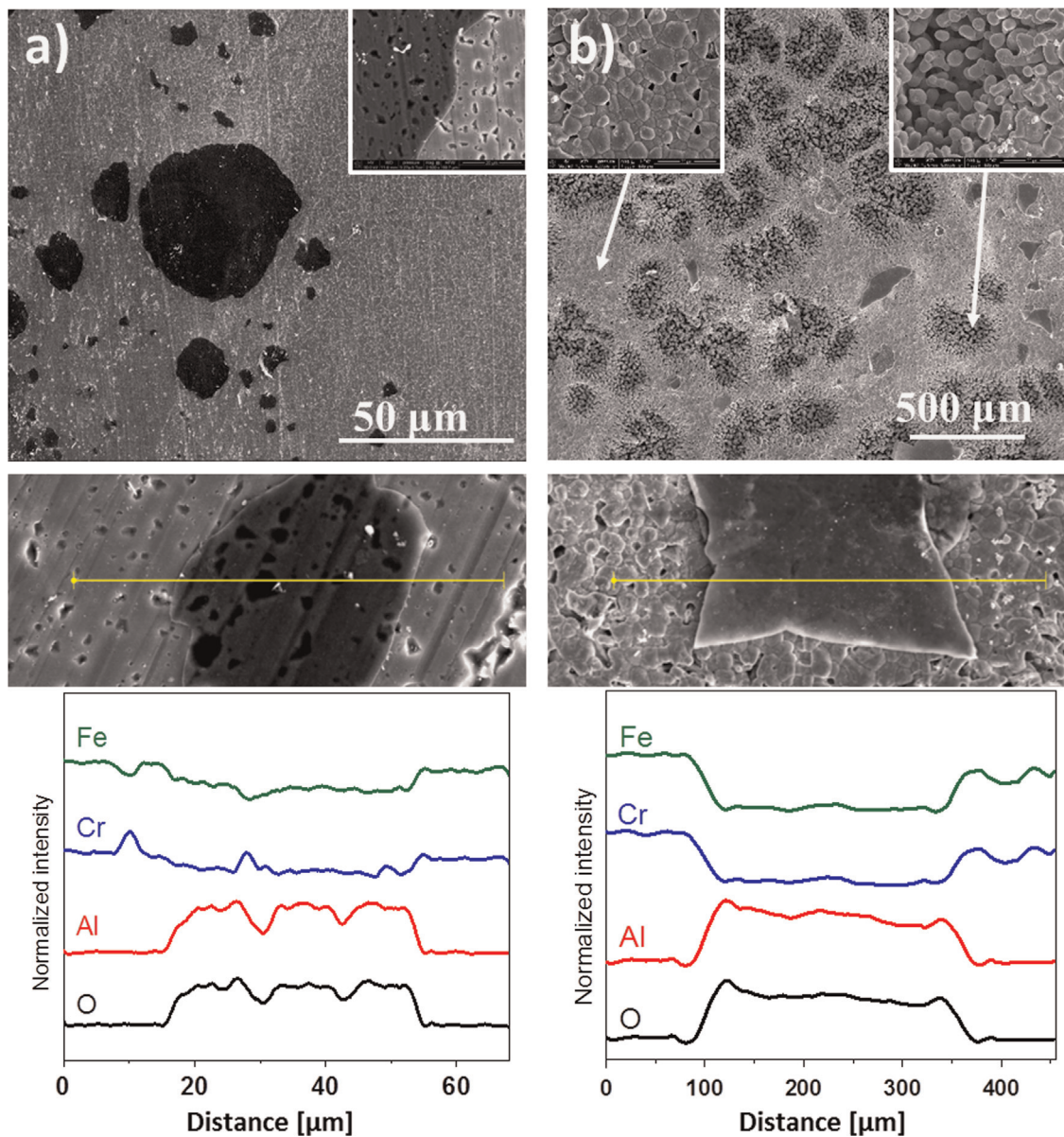


Fig. 13. Surface SEM image of APM sample after exposure to LBE at 700 °C (a) and 800 °C (b); inset higher magnification of representative surface morphologies and EDS line scan of different features.

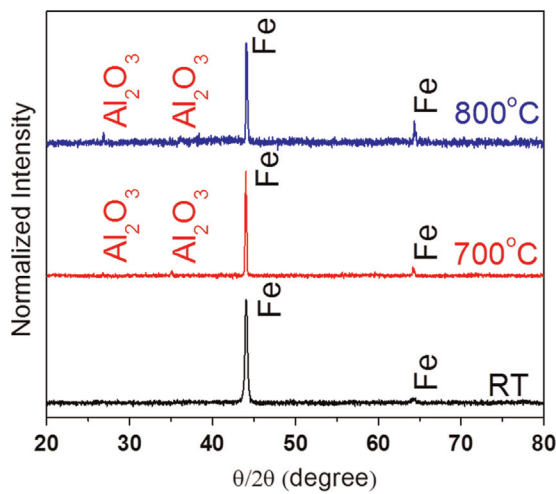


Fig. 14. XRD of sample APM at RT and after exposure to LBE at 700 °C and 800 °C.

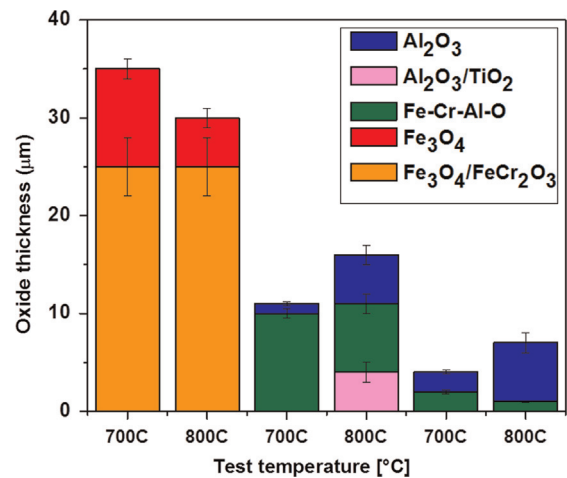


Fig. 15. a) Average oxide thickness layer after exposure to LBE at 700 °C and 800 °C. The error bars indicate a single standard deviation.

The 316L alloy showed the expected behavior of dissolution driven by high Ni solubility in LBE and with a fast-growing non-protective oxide formation. The surface oxide scale formed on FeCrAl alloys offers a good protection, and for the ALK alloy, the Al₂O₃ oxide has superior bonding to the substrate. The uniformly distributed pit-type dissolution of the APM substrate was not unexpected, given the presence of LBE within the oxide scale. The localized dissolution pits indicate an ongoing protective oxide scale delamination during corrosion test.

Three stainless steel materials were used in this work. The corrosion tests were performed for two temperatures and one oxygen concentration. The selection of the 316L steel was as a baseline for comparison with current studies and its poor performance at elevated temperatures indicates that further such studies should only focus on aluminum-containing steels that are more likely to form passivating oxides. Oxygen control at above 700 °C was easily achievable with the current testing setup. More high temperature tests are required for lower oxygen concentrations (10⁻⁶ and 10⁻⁷ wt%) that are more likely to be expected in operational reactors with limited oxygen sources. Lower oxygen concentrations would be expected to form thinner oxide layers but foremost it may allow promoting the higher quality Cr and Al oxides at expense of the Fe–Cr–Al spinel structures that have the tendency to exhibit cracking and delamination. In order to observe in more detail the oxides growth with time, samples will be pulled out at different stages in the corrosion process and evaluated. After optimization of process parameters such as oxide evolution and oxygen concentration, the range of temperature cycling that exists in solar plant containment can be addressed as well.

5. Summary

Longer term exposure of commercial Fe–Cr–Al alloys in LBE at temperatures as high as 800 °C was conducted. The oxygen content in the LBE was controlled and detailed experimental issues associated with the control are highlighted. Relatively stable oxide layers were found and identified. It was found that a transitional inner-layer of Fe–Cr–Al oxides at the substrate interface and an Al-oxide outer layer on the Fe–Cr–Al alloys were formed. As expected, a fast growing non-protective oxide scale with underlying dissolution was observed on the 316L alloy.

Acknowledgement

The authors want to thank the DOE SunShot Program (Grant no. DE-EE0005941) for financial support of this work. We also want to thank Sandwick steel for providing sample materials to conduct these tests.

References

- [1] D. Frazer, E. Stergar, C. Cionea, P. Hosemann, Liquid metal as a heat transport fluid for thermal solar power applications, *Energy Procedia* 49 (2014) 627–636.
- [2] H. Yapici, G. Genc, N. Demir, A comprehensive study on neutronics of a lead–bismuth eutectic cooled accelerator-driven sub-critical system for long-lived fission product transmutation, *Ann. Nucl. Energy* 35 (2008) 1264–1273.
- [3] CRC Handbook of Chemistry and Physics, 95th edition, Internet version, 2015.
- [4] Y. Kurata, Corrosion behavior of cold-worked austenitic stainless steels in liquid lead–bismuth eutectic, *J. Nucl. Mater.* 448 (2014) 239–249.
- [5] P. Hosemann, M. Hawley, D. Koury, J.G. Swadener, J. Welch, A.L. Johnson, G. Mori, N. Li, Characterization of oxide layers grown on D9 austenitic stainless steel in lead bismuth eutectic, *J. Nucl. Mater.* 375 (2008) 323–330.
- [6] E. Yamaki, K. Ginestar, L. Martinelli, Dissolution mechanism of 316L in lead–bismuth eutectic at 500 °C, *Corr. Sci.* 53 (2011) 3075–3085.
- [7] S. Takaya, T. Furukawa, K. Aoto, G. Muller, A. Weisenburger, A. Heitzel, M. Inoue, T. Okuda, F. Abe, S. Ohnuki, T. Fujisawa, A. Kimura, Corrosion behavior of Al-alloying high Cr-ODS steels in lead–bismuth eutectic, *J. Nucl. Mater.* 386–388 (2009) 507–510.
- [8] L. Martinelli, F. Balbaud-Celerier, A. Terlain, S. Bosonnet, G. Picard, G. Santarini, Oxidation mechanism of an Fe–9Cr–1Mo steel by liquid Pb–Bi eutectic alloy at 470 °C (Part II), *Corr. Sci.* 50 (2008) 2537–2548.
- [9] M. Del Giacco, A. Weisenburger, A. Jianu, F. Lang, G. Mueller, Influence of composition and microstructure on the corrosion behavior of different Fe–Cr–Al alloys in molten LBE, *J. Nucl. Mater.* 421 (2012) 39–46.
- [10] M. Kondo, M. Takahashi, T. Suzuki, K. Ishikawa, K. Hata, S. Qiu, H. Sekimoto, Metallurgical study on erosion and corrosion behaviors of steels exposed to liquid lead–bismuth flow, *J. Nucl. Mater.* 343 (2005) 349–359.
- [11] G. Mueller, A. Heinzel, J. Konys, G. Schumacher, A. Weisenburger, F. Zimmermann, V. Engelko, A. Rusanov, V. Markov, Behavior of steels in flowing liquid PbBi eutectic alloy at 420–600 °C after 4000–7200 h, *J. Nucl. Mater.* 335 (2004) 163–168.
- [12] N. Li, Active control of oxygen in molten lead–bismuth eutectic systems to prevent steel corrosion and coolant contamination, *J. Nucl. Mater.* 300 (2002) 73–81.
- [13] A. Weisenburger, K. Aoto, G. Muller, A. Heinzel, G. Schumacher, T. Furukawa, Behavior of chromium steels in liquid Pb–55.5Bi with changing oxygen content and temperature, *J. Nucl. Mater.* 358 (2006) 69–76.
- [14] Z.G. Zhang, F. Gesmundo, P.Y. Hou, Y. Niu, Criteria for the formation of protective Al₂O₃ scales on Fe–Al and Fe–Cr–Al alloys, *Corros. Sci.* 48 (2006) 741–765.
- [15] A. Weisenburger, G. Muller, A. Heinzel, A. Jianu, H. Munscher, M. Kieser, Corrosion, Al containing corrosion barriers and mechanical properties of steels foreseen as structural materials in liquid lead alloys cooled nuclear systems, *Nucl. Eng. Des.* 241 (2011) 1329–1334.
- [16] A. Weisenburger, A. Jianu, S. Doyle, M. Bruns, R. Fetzer, A. Heinzel, M. DelGiacco, W. An, G. Muller, Oxide scale formed on Fe–Cr–Al-based model alloys exposed to oxygen containing molten lead, *J. Nucl. Mater.* 437 (2013) 282–292.
- [17] P. Hosemann, H.T. Thau, A.L. Johnson, S.A. Maloy, N. Li, Corrosion of ODS steels in lead–bismuth eutectic, *J. Nucl. Mater.* 373 (2008) 246–253.
- [18] Handbook on lead–bismuth alloy and lead properties, materials compatibility, thermal hydraulics and technologies, ISBN:978-92-64-99002-9, 2007.
- [19] A.M. Bolind, A.P. Shivprasad, D. Frazer, P. Hosemann, Essential aspects of controlling the oxygen content of molten tin in engineering applications, *Mater. Des.* 52 (2013) 168–178.
- [20] D. Koury, A.L. Johnson, T. Ho, J.W. Farley, Analysis of bi-layer oxide on austenitic stainless steel, 316L, exposed to lead–bismuth eutectic (LBE) by X-ray photoelectron spectroscopy (XPS), *J. Nucl. Mater.* 440 (2013) 28–33.
- [21] A.M. Jubb, H.C. Allen, Vibrational spectroscopic characterization of hematite, maghemite, and magnetite thin films produced by vapor deposition, *ACS Appl. Mater. Interfaces* 2 (2010) 2804–2812.
- [22] K.F. McCarty, D.R. Boehme, A Raman study of the systems Fe_{3-x}Cr_xO₄ and Fe_{2-x}Cr_xO₃, *J. Solid State Chem.* 79 (1989) 19–27.
- [23] M. Gao, W. Li, J. Dong, Z. Zhang, B. Yang, Synthesis and characterization of superparamagnetic Fe₃O₄@SiO₂ core–shell composite nanoparticles, *WJCPM* 1 (2011) 49–54.
- [24] A. Wang, K.E. Kuebler, B.L. Jolliff, L.A. Haskin, Raman spectroscopy of Fe–Ti–Cr–oxides, case study: martian meteorite EETA 79901, *Am. Mineral.* 89 (2004) 665–680.
- [25] B.D. Hosterman, Raman Spectroscopy Study of Solid Solution Spinel Oxides, UNLV Theses/Dissertations/Professional/Papers/Capstones, Paper 1087, 2011.
- [26] G.M. Muller, G. Schumacher, F. Zimmermann, Investigation on oxygen controlled liquid lead corrosion of surface treated steels, *J. Nucl. Mater.* 278 (2000) 85–95.
- [27] C. Badini, F. Laurella, Oxidation of FeCrAl alloy: influence of temperature and atmosphere on scale growth rate and mechanism, *Surf. Coat. Technol.* 135 (2001) 291–298.
- [28] G. Hilson, K.R. Hallan, P.E.J. Flewitt, The measurement of stresses within oxides produced on austenitic and ferritic steels using Raman spectroscopy, *Mater. Sci. Forum* 524–525 (2006) 957–962.
- [29] L. Gasparov, T. Jegorek, L. Loetgering, S. Middey, J. Chakhalian, Thin film substrates from the Raman spectroscopy point of view, *J. Raman Spectrosc.* 45 (2014) 465–469.
- [30] U. Balachandran, N.G. Eror, Raman spectra of titanium dioxide, *J. Solid State Chem.* 42 (1982) 276–282.
- [31] G.A. Tompsett, G.A. Bowmaker, R.P. Cooney, J.B. Metson, K.A. Rodgers, J.M. Seakins, The Raman spectrum of brookite, TiO₂ (Pbca, Z = 8), *J. Raman Spectrosc.* 26 (1995) 57.
- [32] W. Fei, S.C. Kuiry, S. Seal, Inhibition of metastable alumina formation on Fe–Cr–Al–Y alloy fibers at high temperature using titania coating, *Oxid. Met.* 62 (2004) 29–44.
- [33] X. Chen, J.F. Stubbins, P. Hosemann, A.M. Bolind, Analysis of corrosion scale structure of pre-oxidized stainless steel 316 in molten lead bismuth eutectic and the relation to impedance spectroscopy response, *J. Nucl. Mater.* 398 (2010) 172–179.
- [34] C. Schroer, O. Wedemeyer, J. Novotny, A. Skrypnik, J. Konys, Selective leaching of nickel and chromium from Type 316 austenitic steel in oxygen-containing lead–bismuth eutectic (LBE), *Corros. Sci.* 84 (2014) 113–124.
- [35] J. Lim, H.O. Nam, I.S. Hwang, J.H. Kim, A study of early corrosion behaviors of FeCrAl alloys in liquid lead–bismuth eutectic environments, *J. Nucl. Mater.* 407 (2010) 205–210.

- [36] C. Wagner, Passivity and inhibition during the oxidation of metals at elevated temperature, *Corros. Sci.* 5 (11) (1965) 751–764.
- [37] J. Young, High temperature oxidation and corrosion of metals. Oxidation of alloys I: single phase scales, *Elsevier* 1 (5) (2008) 185–246.
- [38] Y. Niu, S. Wang, F. Gao, Z.G. Zhang, F. Gesmundo, The nature of the third-element effect in the oxidation of Fe-xCr-3 at% Al alloys in 1 atm O₂ at 1000 °C, *Corros. Sci.* 50 (2008) 345–356.
- [39] D. Naumenko, W.J. Quadakkers, A. Galerie, Y. Wouters, S. Jourdain, Parameters affecting transient oxide formation on FeCrAl based foil and fibre materials, *Mater. High Temp.* 20 (3) (2003) 287–293.
- [40] R. Prescott, M.J. Graham, The formation of aluminum oxide scales on high-temperature alloys, *Oxid. Met.* 38 (1992) 233–254.
- [41] X. Chen, R. Haasch, J.F. Stubbins, Impedance spectroscopy and microstructural characterization of the corrosion behavior of FeCrAl alloys in lead–bismuth eutectic, *J. Nucl. Mater.* 431 (2012) 125–132.
- [42] K.M.N. Prasanna, A.S. Khanna, R. Chandra, W.J. Quadakkers, Effect of θ-alumina formation on the growth kinetics of alumina-forming superalloys, *Oxid. Met.* 46 (1996) 465–480.
- [43] B.A. Pint, M. Treska, L.W. Hobbs, The effect of various oxide dispersions on the phase composition and morphology of Al2O3 scales grown on NiAl, *Oxid. Met.* 47 (1997) 1–20.
- [44] P. Burtin, J.P. Brunelle, M. Pijolat, M. Soustelle, Influence of surface area and additives on the thermal stability of transition alumina catalyst supports. I: kinetic data, *Appl. Catal.* 34 (1987) 225.